Nanoscale

Real-time imaging and elemental mapping of AgAu nanoparticle transformations†

E. A. Lewis,[a] T. J. A. Slater,[a] E. Prestat,[a] A. Macedo,[b] P. O'Brien,[c] P. H. C. Camargo*[b] and S. J. Haigh*[a]

We report the controlled alloying, oxidation, and subsequent reduction of individual AgAu nanoparticles in the scanning transmission electron microscope (STEM). Through sequential application of electron beam induced oxidation and *in situ* heating and quenching, we demonstrate the transformation of Ag–Au core–shell nanoparticles into: AgAu alloyed, Au–Ag core–shell, hollow Au–Ag₂O core–shell, and Au–Ag₂O yolk-shell nanoparticles. We are able to directly image these morphological transformations in real-time at atomic resolution and perform energy dispersive X-ray (EDX) spectrum imaging to map changing elemental distributions with sub-nanometre resolution. By combining aberration corrected STEM imaging and high efficiency EDX spectroscopy we are able to quantify not only the growth and coalescence of Kirkendall voids during oxidation but also the compositional changes occurring during this reaction. This is the first time that it has been possible to track the changing distribution of elements in an individual nanoparticle undergoing oxidation driven shell growth and hollowing.

1. Introduction

Control of elemental segregation in metallic nanoparticles is important for understanding composition dependent optical and catalytic properties in a wide range of applications.[1–6] Galvanic replacement provides a simple low temperature synthesis route for producing metallic nanoparticles with different elemental distributions.[1] Galvanic reactions can be employed in combination with the nanoscale Kirkendall effect, to synthesize noble metal nanoparticles with hierarchical elemental distributions and complex hollow morphologies.[2] The nanoscale Kirkendall effect also provides an effective means of producing porous metal oxides, sulphides, phosphides, nitrides, and selenides with critical dimensions on the order of nanometres from solid metal starting materials by harnessing a difference in the diffusion rates of two elements across an interface.[7–16] This diffusional imbalance produces a net flow of matter countered by an opposing flow of vacancies that can coalesce to form voids.[9,17] The nanoscale Kirkendall effect thus provides an important synthetic route for an extensive

range of semiconducting and heterostructured nanocrystals with complex internal porosity and unusual morphologies.[9,18,19]

The majority of studies into the nanoscale Kirkendall effect are limited to monometallic starting materials.[8,12,13,20,21] However, there has also been interest in using bimetallic starting materials to synthesise metal-semiconductor hybrid materials with novel morphologies.[9,22–24] Pt-core Co-shell particles have been oxidised to form Pt-yolk CoO-shell structures,[9,22] FePt-core Co-shell particles have been reacted with a sulphur containing solution to form FePt-yolk CoS₂-shell particles,[23] and Au-core Fe-shell particles have been oxidised to form particles with an Au-core and hollow Fe₂O₃-shell.[24]

The capability to synthesise nanostructures containing both a metal and semiconductor component is important for many applications, as it provides a route to harness the complementary functionality of two dissimilar materials. One important example is in biomedical imaging, where properties of the two materials can be combined to create multimodal probes:[25,26] Au-core Fe₂O₃-shell particles have potential as dual MRI, X-ray contrast agents;[24] Au–ZnO hybrids may be used for fluorescence biolabelling;[27] and Co-core CdSe-shell particles are both magnetic and luminescent.[26] Another application of metal-semiconductor hybrid nanostructures is in photocatalysis; photoexcitation can occur in the semiconductor region which subsequently leads to charge accumulating in the metal region which can promote reduction reactions.[28]

Despite the many examples of successful synthesis *via* the nanoscale Kirkendall effect, the dynamics of these reactions

[a] *School of Materials, The University of Manchester, Manchester, M13 9PL, UK. E-mail: Sarah.Haigh@mancester.ac.uk*
[b] *Departamento de Química Fundamental, Instituto de Química, Universidade de São Paulo, São Paulo 05508-000, Brazil. E-mail: camargo@iq.usp.br*
[c] *School of Materials and School of Chemistry, The University of Manchester, Manchester M13 9PL, UK*
† Electronic supplementary information (ESI) available. See DOI: 10.1039/c4nr04837g

for individual nanostructures are largely unexplored. Progress has been made in two recent studies which have employed low resolution TEM imaging and *ex situ* elemental mapping to investigate the oxidation of Bi and Ni–Cr nanoparticles.[29,30] Here we are able to go beyond *in situ* imaging, employing recent technological advances in high efficiency EDX detectors for the STEM in order to monitor changes in elemental distribution for individual nanoparticles during dynamic transformations.

We have applied this approach in order to make the first observations of the transformation of bimetallic Ag–Au nanoparticles starting materials to hollow Au-core Ag_2O-shell nanostructures *via* the nanoscale Kirkendall effect. We investigate the importance of the spatial distribution of Au and Ag in the starting material over the product formation by studying both Au surface segregated and homogeneously alloyed AgAu nanoparticles under identical reaction conditions. Furthermore, we demonstrate that by employing low temperature oxidation followed by moderate heating the Au surface segregated nanoparticles can be inverted to an Au-core Ag-shell structure, which can then be further oxidized to form Au-yolk Ag_2O-shell particles.

2. Experimental section

Ag–Au core–shell particles were prepared using the galvanic replacement reaction, using a procedure detailed in previous work.[1] Aqueous solutions of the nanoparticles were drop cast onto TEM membranes and allowed to dry before imaging. For standard beam induced oxidation reactions 30 nm thick Si_3N_4 membranes (Agar Scientific, UK) were used, for experiments involving *in situ* heating specific heating chips were used. For *in situ* heating experiments dedicated TEM holders designed to be used with *Micro-Electro-Mechanical Systems* (MEMS) chips were used. *In situ* heating was performed using a Protochips Aduro heating holder in conjunction with Protochips Aduro Thermal E-chips with both 50 nm Si_3N_4 (E-AHA11) and amorphous carbon (E-AHA21) support membranes. *In situ* heating was also performed using a DENSsolutions sample heating system with DENSsolutions EMheaterchips™ Si_3N_4 chips.

High angle annular dark field (HAADF) scanning transmission electron microscope (STEM) images and energy dispersive X-ray (EDX) spectrum images were acquired using a probe-side aberration corrected FEI Titan G2 80-200 S/TEM "ChemiSTEM™" instrument operated at 200 kV. Images and spectrum images were acquired with a probe current of ~200 pA and a convergence semi-angle of 18.5 mrad. HAADF imaging was performed with an inner collection semi-angle of 54 mrad. Spectrum images were acquired with all four SSD detectors turned on and the sample un-tilted.

STEM images were recorded using FEI TIA software. Automated image analysis of void growth and coalescence was performed using ImageJ software. EDX spectroscopy data was recorded using Bruker Esprit software and quantified using the Cliff-Lorimer approach without absorption correction.

3. Results and discussion

3.1 Direct observation of the nanoscale Kirkendall effect

When Au surface segregated AgAu nanoparticles, synthesised by galvanic replacement,[1] are exposed to electron beam irradiation at dose rates above approximately 2000 e $Å^{-2}$ s^{-1}, high angle annular dark field (HAADF) STEM imaging reveals the dramatic morphological transformation of a single bimetallic nanoparticle (Fig. 1a–f). In the early stages of the transformation, isolated regions of new material grow on the surface of the particle (Fig. 1b and c and video S1†), such multi-site oxide nucleation has previously been observed in the oxidation of Ni–Cr nanoparticles.[30] As the reaction proceeds, these regions increase in size and appear to cover the whole nanoparticle surface, forming a shell (Fig. 1d–f). In parallel, multiple voids appear in the particle's core during the early stages of the reaction (Fig. 1d), which grow and eventually coalesce (Fig. 1e and f and video S2†). Similar transformations were observed for all nanoparticles studied in the same system (Fig. S1†).

The nucleation and coalescence of voids inside the nanoparticle is consistent with the mechanism proposed in previous reports of the nanoscale Kirkendall effect.[9,13,21] Our *in situ* STEM imaging results provide not only a direct confirmation of this process for a bimetallic system but also allow quantitative analysis of void growth and coalescence using automated image analysis of sequential HAADF STEM images (Fig. 1j with further details in ESI Fig. S2†). Here we observe an approximately constant areal growth rate for the total void area (~0.74 nm^2 s^{-1}) accompanied by a decrease in the number of discreet voids, from four to one, as neighbouring voids combine.

3.2 *In situ* EDX spectrum imaging

Although the contrast of the HAADF images scales directly with atomic number and sample thickness,[31,32] contrast differences can be difficult to interpret for complex morphologies like those observed for bimetallic nanoparticles synthesised *via* the galvanic replacement reaction.[1] Complementary EDX spectrum imaging of the same particle at different stages of this process allows the morphological changes observed in the *in situ* HAADF images to be directly related to compositional variations. The EDX spectrum images of the particle before the transformation begins reveals that initially particles display clear Au surface segregation (Fig. 1g, corresponding to HAADF image Fig. 1a), with a composition of ~7 at% Au 93 at% Ag. The EDX spectrum image taken after an electron dose of approximately 3.6 × 10^6 e $Å^{-2}$ (Fig. 1h, corresponding to HAADF image Fig. 1c) clearly demonstrates that the shell grown is silver and oxygen rich while Au has diffused inwards into the core. After an even greater electron dose of approximately 7.1 × 10^6 e $Å^{-2}$ the EDX spectrum image and accompanying line scans (Fig. 1i, corresponding to HAADF image Fig. 1f) reveal further inward diffusion of Au. The diameter of the region containing Au decreases from approximately 31 nm to 23 nm between Fig. 1g and 1i. The distribution of Ag and O
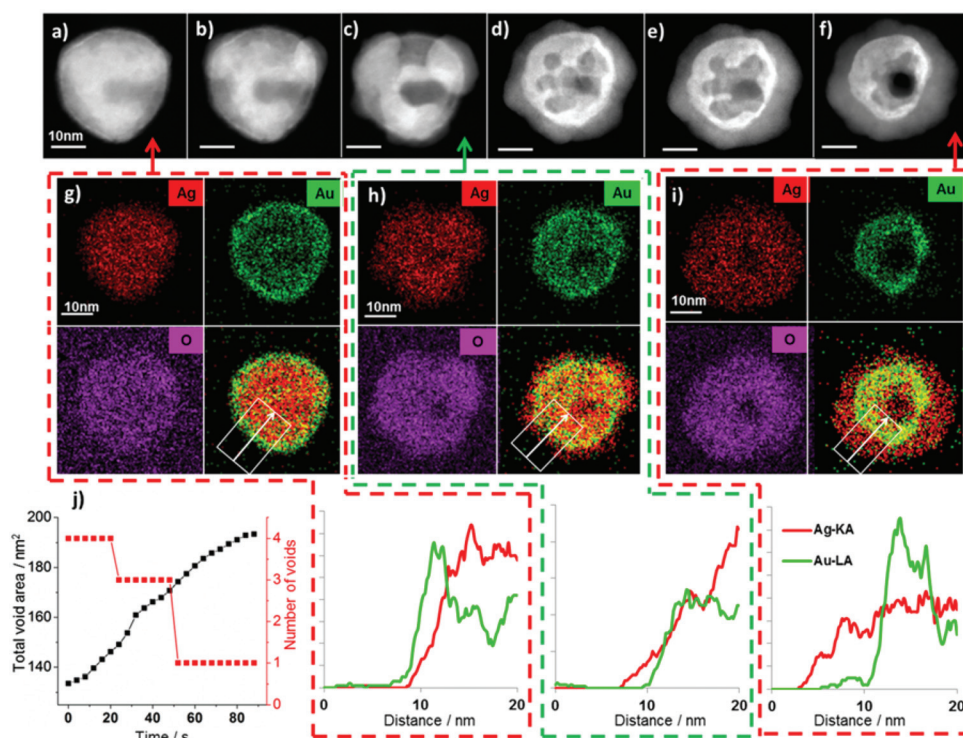
Fig. 1 (a–f) HAADF STEM images showing the transformation of a single nanoparticle, from an Au surface segregated Ag–Au structure to a hollow Au-core Ag_2O-shell structure. (g–i) EDX spectrum images acquired at different stages of the process reveal the compositional changes associated with the morphological changes visible in the HAADF images. The elemental maps in (g) correspond to the period between (a) and (b), (h) corresponds to the period between (c) and (d), and (i) corresponds to the period between (e) and (f). Videos of image sequences acquired between (b) and (c) and between (d) and (e) can be found in the ESI (videos S1 and S2† respectively). The process is accompanied by a dramatic increase in the oxygen signal (with the O/Ag at% ratio, found by EDX quantification, increasing 153% from 0.86 to 2.18), implying the transformation is driven by oxidation. (j) shows quantitative analysis of void growth and coalescence gained by automated image analysis of HAADF STEM image sequences acquired between (d) and (e) (ESI Fig. S2 and video S2†).

signals (Fig. 1g–i) shows that the location of these two elements are strongly correlated, and quantitative analysis of the full summed EDX spectrum images (Fig. 1g and 1i) reveals that the transformation is accompanied by a dramatic increase in oxygen (O/Ag at% ratio) of 153%. In contrast, quantification of the Au/Ag ratio for the full summed EDX spectrum images reveals this remains constant during the transformation. Spectrum imaging of beam induced shell growth and void formation in a second particle reveals similar changes in elemental distribution and oxygen signal (ESI Fig. S3†).

The increased oxygen signal suggests that shell growth is a consequence of silver oxide formation at the surface of the particle, as illustrated schematically in Fig. 2. It is proposed that the dramatic morphological changes seen here are characteristic of the nanoscale Kirkendall effect. The formation of silver oxide at the surface of the nanoparticles, coupled with the faster diffusivity of Ag compared to O, produces an increased concentration of vacancies internally which coalesce to form voids. This nanoscale Kirkendall effect has previously been employed to synthesise hollow Ag_2S and Ag_2Se nanostructures from silver nanoparticles in thiourea and CeS_2 solutions respectively.[33–35] It has also been shown to allow production of many different hollow metal oxide nanostructures,[13,20,24,29,36]
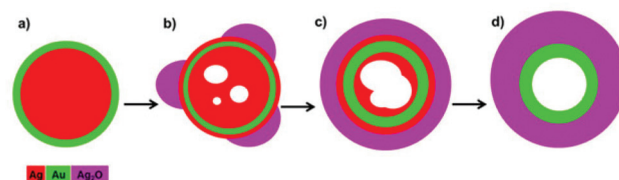

Fig. 2 Illustration of observed structural transformations: (a) Au surface segregated starting structure, (b) beam induced oxidation results in Ag_2O formation, with oxide nucleating at multiple sites on the particle's surface. Ag diffuses faster than O through AgAu resulting in outward diffusion of Ag and an increased concentration of vacancies in the core which drives both inward diffusion of Au and the nucleation of voids. (c) Ag_2O islands grow so as to cover the whole surface, continued injection of vacancies into the core result in void growth and further inward diffusion of Au. (d) The final structure has a thick Ag_2O shell, the voids in the core have coalesced, and Au is now concentrated in the centre of the particle.

however, to the best of our knowledge, this is the first example involving the oxidation of silver to silver oxide.

Whilst many examples of electron beam induced chemical transformations involve reduction or localised heating,[37–40] the electron beam has also previously been observed to drive the oxidation of Co nanoparticles, resulting in Co-core

CoO-shell particles.[41] It was proposed that reactive O species were generated by the interaction of the electron beam with carboxylic groups on the surface of the Co particles.[41] We postulate that an analogous oxidation reaction occurs here with the electron beam interacting with polyvinylpyrrolidone (PVP) molecules, remaining from synthesis, to generate reactive O species (for further discussion of the oxidation mechanism see ESI†).

3.3 Atomic resolution imaging

Au and Ag both have a similar structure and lattice constant, meaning that is it not possible to distinguish these two elements by analysis of the interplanar distances present in high resolution TEM images. As expected high resolution HAADF STEM images of the starting structures initially show only lattice spacings that are consistent with interplanar distances of both Au and Ag (Fig. 3d and f). However, after beam

Fig. 3 HAADF STEM images (a–c) show the evolution of an Ag–Au particle under election beam irradiation. (d) and (e) show high resolution images of this particle, with (d) taken just after (a) and (e) taken between (b) and (c), Fourier transforms for these images are shown inset and the areas highlighted by red boxes are shown enlarged below in (f) and (g) together with identified lattice spacings. The structure before transformation ((a), (d) and (f)) displays only lattice spacings corresponding to Ag and Au ({111} spacing of both Ag and Au ~0.24 nm) while the structure after beam induced shell growth ((b), (e) and (g)) clearly shows lattice spacing corresponding to Ag_2O ({111} ~0.27 nm and {110} ~0.33 nm). Corresponding EDX spectrum images can be found in ESI (Fig. S4†).

induced shell growth takes place, larger lattice spacings of ~0.27 nm and ~0.33 nm are observed, corresponding to the {111} and {110} Ag_2O planes respectively (Fig. 3e and g) and providing further evidence that the formed shell is composed of silver oxide.

3.4 Substrate dependence of nanoparticle oxidation

In all of the experimental observations presented so far the nanoparticles were supported on a silicon nitride membrane. The relatively high vacuum of the TEM (~10^{-5} Pa) supports the hypothesis that oxidising species are supplied by polyvinylpyrrolidone (PVP) found on the surface of the particles and the surrounding substrate (see ESI†). It is therefore important to note that no oxidation occurred under the same irradiation conditions when experiments were repeated using identical nanoparticles on an amorphous carbon support (Fig. S5†). At first this is perhaps surprising, as after electron beam irradiation high concentrations of oxygen were detected on the amorphous carbon support, with EDX spectroscopy measurements of comparable regions showing 121% greater O/Ag at% ratio associated with the carbon support compared to a silicon nitride support membrane (Fig. S5†). We therefore postulate that the chemical inertness of Si_3N_4 contributes to facilitate the oxidation of silver. There is a ready supply of oxygen containing species on both types of support and it is known that the electron beam attracts such species, increasing the localised oxygen concentration in the vicinity of the nanoparticle under investigation. EDX elemental mapping demonstrates that on silicon nitride, this increased oxygen signal is clearly associated with the particles, whereas on amorphous carbon the increased oxygen signal is correlated with the support (Fig. S5†). It has been previously shown that amorphous carbon can be oxidised to form a range of carbonyl species in place of the original C–H bonds found on its surface.[42] We therefore suggest that the reactive oxygen species oxidise the amorphous carbon substrate more readily than the Ag, whereas on the more chemically inert Si_3N_4 substrate the reverse is true.

Further insights into the observed transformation may be obtained by consideration of the different behaviour of the two metals present in the starting materials. Au is considerably less susceptible to oxidation than silver, the standard reduction potentials of Ag^+ and Au^{3+} are 0.7996 V and 1.498 V respectively. It is therefore not unexpected that above a critical electron dose rate Ag is readily oxidised while Au remains metallic. These two metals also have different diffusion constants, the diffusivity of Ag in an AgAu solid solution being 2–3 times greater than that of Au.[43] Inward diffusion of Au is observed, driven by vacancies in the core, however, gold cannot diffuse into the core as rapidly as silver can diffuse out of it and this imbalance causes a build-up of vacancies in the core, which coalesce to form voids.[2,43] As the particles studied typically contain ~6 at% Au and ~94 at% Ag, there is considerably more silver present than gold, enhancing the diffusional imbalance.
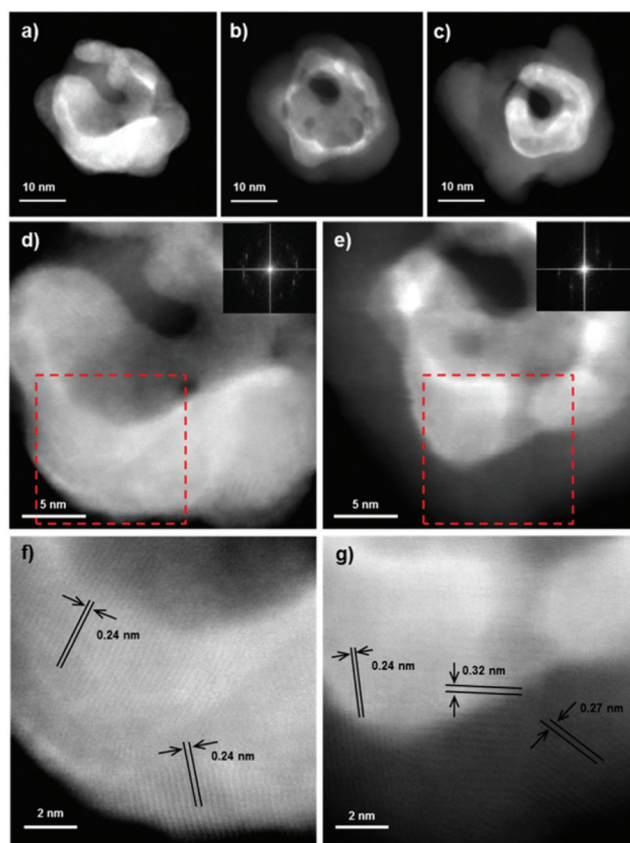
3.5 Comparison of alloyed and core–shell starting materials through *in situ* heating

The presence of an initial Au-rich surface in the system studied in Fig. 1 raises the possibility that Au surface segregation plays a role in the phenomenon observed. To clarify the importance of the initial elemental distribution on the subsequent oxidation reaction we have investigated the dynamics of this reaction for alloyed nanoparticles with otherwise identical structure and compositions.

AgAu alloys form a thermodynamically stable face centred cubic solid solution at all compositions in the bulk.[43,44] Our Au surface segregated starting structure is therefore a metastable state which, with sufficient thermal energy, can be transformed into a homogenous alloy. Modern TEM heating holders employ membrane based heaters with low thermal mass to produce rapid local *in situ* heating and quenching of samples with minimal drift.[45] These holders also allow the acquisition of EDX spectroscopy data at elevated temperatures and therefore facilitate investigation into the effect of temperature on elemental distributions in nanomaterials.[46] *In situ* heating of the AgAu nanoparticles with Au surface segregation to 400 °C brings about rapid and complete alloying with little change in the particle morphology and no change in their overall composition (Fig. 4b). While imaging at 400 °C the particles are unreactive and no Ag$_2$O shell growth or void formation is observed for the newly formed alloyed particles,

even at dose rates above 2000 e Å^{-2} s^{-1}. This supports our hypothesis that the reaction is due to beam induced creation of oxidising species rather than beam induced heating of the sample.

When the alloyed nanoparticles are quenched to room temperature their newly alloyed structure is retained (Fig. 4c). However, when the newly alloyed nanoparticles are exposed to electron beam irradiation above the threshold dose rate at room temperature Ag$_2$O formation occurs. Therefore, it is clear that the stability observed at 400 °C is a consequence of the elevated temperature rather than the change in elemental distribution. Indeed, the alloyed particles display an identical pathway of Ag$_2$O shell growth and void formation to that observed for the Au surface segregated system (Fig. 4c–e). For the ensemble of particles shown in Fig. 4, quantification of the summed EDX spectra extracted from the full spectrum images reveals that during heating to 400 °C, quenching and subsequent oxidation the Au : Ag ratio remains constant (94 at% Ag, 6 at% Au). In contrast, the O : Ag ratio more than doubles during oxidation, with the majority of the oxygen content associated with the nanoparticle shell (Fig. 4f and ESI Fig. S6†).

The temperature dependence observed here can be simply explained; silver oxide is known to be unstable at elevated temperatures and would be expected to completely decompose to metallic silver and oxygen at 400 °C.[47–49] The thermodynamic driving force for oxidation of silver is greater at lower temperatures, although the precise free energy change is highly dependent on particle size.[50] Thermodynamic calculations predict that oxidation of Ag nanoparticles is only favourable at 400 °C when a particle's radius is <7 nm (considerably smaller than our particles).[50] The *in situ* heating results suggest that the initial distribution of silver and gold in the particles is of little consequence to subsequent oxidation and void formation.

3.6 Core–shell inversion and yolk-shell formation through sequential *in situ* heating and beam induced oxidation

Hollow nanostructures are predicted to be unstable relative to solid forms.[51,52] In addition, Ag$_2$O is known to be unstable with respect to metallic silver and oxygen at elevated temperatures.[47] When the hollow Au–Ag$_2$O structures, formed by the electron beam irradiation of Ag–Au particles (Fig. 5a–c and g) are heated, the loss of the hollow interior and an apparent shrinking of the shell is observed (Fig. 5d and h). This transformation is accompanied by a modest decrease in the oxygen signal (O/Ag at% ratio) which suggests that the Ag$_2$O has been fully or partially reduced, forming a particle with a solid Au-rich core and a shell containing metallic Ag (Fig. 5f). Thus, by a combination of the beam induced Kirkendall effect and subsequent heating it is possible to perform something akin to a core–shell inversion, going from an Au-rich surface to an Au-core Ag-shell structure for the same nanoparticle. Once the newly formed Au–Ag core–shell nanoparticle is returned to room temperature, the electron beam is once again able to initiate shell growth (Fig. 5e and i), which is accompanied by a significant increase in the oxygen signal. This supports the
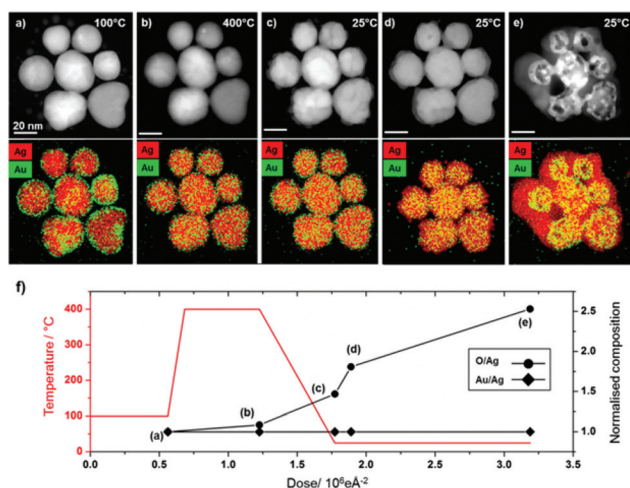

Fig. 4 Homogeneously alloyed AgAu particles, formed by *in situ* heating of Au surface segregated particles, undergo the same Kirkendall transformations as surface segregated particles at room temperature (video S3†) but are unreactive at elevated temperature (400 °C). (a–e) HAADF STEM images (top row) and simultaneously acquired EDX spectrum images (second row, Ag = red and Au = green). (a) At 100 °C all particles initially show Au surface segregation, (b) upon heating to 400 °C homogeneous alloying occurs but no oxidation reaction occurs, on quenching to room temperature a beam induced process of Ag$_2$O shell growth and Au core-hollowing is observed (c–e). Heating to higher temperatures can lead to preferential loss of silver, localised melting and dramatic changes in morphology (Fig. S7†). (f) Graph showing changes to elemental ratios (O/Ag and Au/Ag) as a function of imaging conditions (electron dose and temperature).
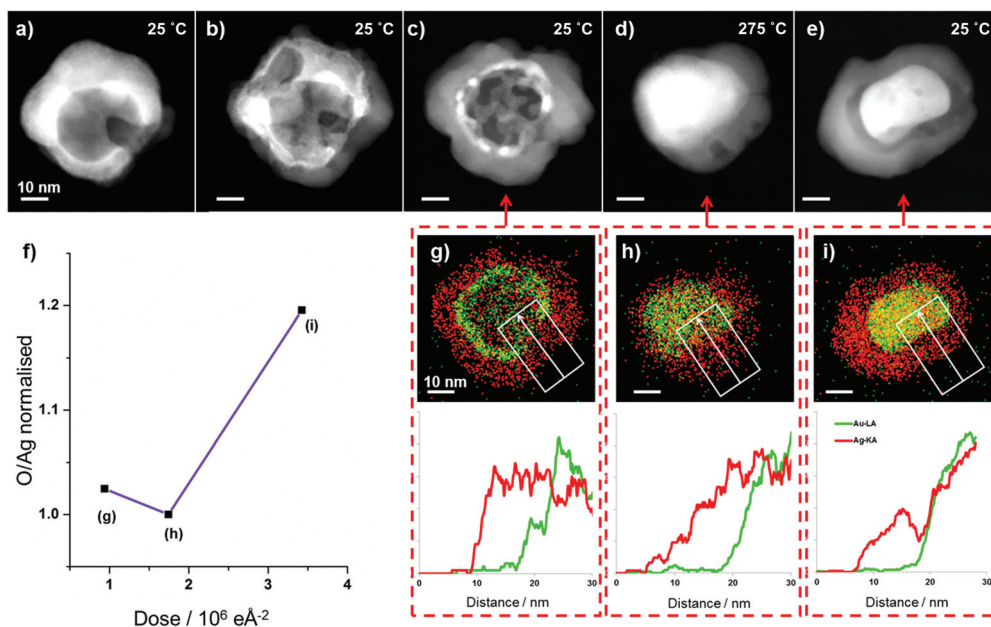
Fig. 5 (a–c) HAADF images showing an Ag–Au particle undergoing the beam induced oxidation reaction described previously, forming a hollow Au–Ag_2O structure. Upon heating to ~275 °C the hollow structure is lost (d), the shell shrinks and EDX data (f) shows a reduced oxygen signal suggesting some Ag_2O is reduced to silver metal. The post heating, non-hollow, Au-core Ag-shell particle ((d) and (h)) undergoes a second beam induced oxidation reaction, in this reaction a yolk-shell (Au-yolk, Ag_2O-shell) particle is formed ((e) and (i)).

idea that heating promotes reduction of Ag_2O to Ag, which can then be re-oxidised by the electron beam at room temperature.

The second oxidation reaction is notably different from the first, no void formation is observed in the core of the particle. Instead we form a yolk-shell structure with voids growing at the interface between the Au-rich core and the Ag-rich shell. This is consistent with previous work on the nanoscale Kirkendall effect where core–shell particles with an inert core material and reactive shell have been oxidised to produce metal-yolk, metal oxide-shell structures.[9,22,53] The development of this yolk-shell structure is evidenced by the linescans taken from spectrum images (Fig. 5g–i): the final yolk-shell structure shows a clear depletion in Ag counts at the edge of the Au rich core (Fig. 5i), no such depletion was present in the initial post-heating structure (Fig. 5h).

4. Conclusions

Electron beam irradiation and *in situ* heating allow us to perform highly controlled oxidation, reduction, and alloying on individual nanoparticles in the STEM. We are able to directly observe the resulting morphological changes at atomic resolution and map changes in elemental distribution at sub-nanometre resolution with EDX spectrum imaging. As summarised in Fig. 6, simple combinations of room temperature oxidation and heating allow us to perform an impressive range of morphological, chemical and structural transformations. We have imaged the real-time oxidation of bimetallic AgAu nanoparticles with different starting elemental distributions and their subsequent reduction by heating, performing
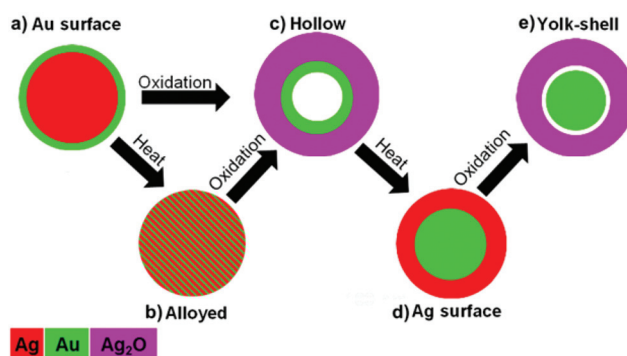

Fig. 6 AgAu bimetallic nanoparticles can undergo a range of controlled *in situ* transformations by sequential application of beam induced oxidation and heating. Au surface segregated AgAu nanoparticles (a) are transformed into alloyed AgAu nanoparticle (b) by heating. Both alloyed (b) and Au surface segregated (a) AgAu nanoparticles can be transformed by electron beam induced oxidation into hollow Au-core Ag_2O-shell structures (c), which can then be reduced to an Au-core Ag-shell structure (d) by heating. Au-core Ag-shell nanoparticles can be oxidised to from Au-yolk Ag_2O-shell structures (e).

core–shell inversion. In materials with significant Au surface segregation as well as those with homogeneous alloying, we observe Ag_2O shell growth, inward diffusion of gold, and the growth and coalescence of voids in the core. Real-time imaging of this process allows quantitative analysis of void growth and coalescence in individual nanoparticles. This work shows, for the first time, that it is possible to produce hollow silver oxide nanostructures by oxidising solid silver-containing particles. Given the interest in silver oxide for catalytic, photovoltaic,

sensing, and antibacterial application,[54–58] we believe the observations presented here could inspire efforts to synthesise hollow silver oxide particles by the nanoscale Kirkendall effect on a laboratory scale. Heating Au surface segregated particles transforms them into alloyed particles, which has little effect on the course of the reaction, with both alloyed and segregated particles showing identical behaviour, forming hollow Au-core Ag_2O-shell structures. In contrast, the inverted Au-core Ag-shell structures oxidize to form Au-yolk Ag_2O-shell structures. In all cases, *in situ* observations of the dynamics of elemental redistribution are characteristic of the nanoscale Kirkendall effect, due to the rapid diffusion of Ag but slow diffusion of O through AgAu. These *in situ* results produce unprecedented insights into the mechanism and reaction kinetics of this important approach to nanoparticle synthesis. Furthermore, this study highlights interesting possibilities for further investigations into the dynamics of nanoparticle reactions using *in situ* STEM EDX spectroscopy, particularly for mixed metal systems.

Acknowledgements

Notes and references

1 T. J. A. Slater, A. Macedo, S. L. M. Schroeder, M. G. Burke, P. O'Brien, P. H. C. Camargo and S. J. Haigh, *Nano Lett.*, 2014, **14**, 1921–1926.

2 E. Gonzalez, J. Arbiol and V. F. Puntes, *Science*, 2011, **334**, 1377–1380.

3 C. Cui, L. Gan, M. Heggen, S. Rudi and P. Strasser, *Nat. Mater.*, 2013, **12**, 765–771.

4 C. Gao, Y. Hu, M. Wang, M. Chi and Y. Yin, *J. Am. Chem. Soc.*, 2014, **136**, 7474–7479.

5 X. Li, Q. Chen, I. McCue, J. Snyder, P. Crozier, J. Erlebacher and K. Sieradzki, *Nano Lett.*, 2014, **14**, 2569–2577.

6 B. Goris, L. Polavarapu, S. Bals, G. Van Tendeloo and L. M. Liz-Marzán, *Nano Lett.*, 2014, **14**, 3220–3226.

7 S. R. Chun, W. A. Sasangka, M. Z. Ng, Q. Liu, A. Du, J. Zhu, C. M. Ng, Z. Q. Liu, S. Y. Chiam and C. L. Gan, *Small*, 2013, **9**, 2546–2552.

8 A. A. El Mel, M. Buffière, P. Y. Tessier, S. Konstantinidis, W. Xu, K. Du, I. Wathuthanthri, C. H. Choi, C. Bittencourt and R. Snyders, *Small*, 2013, **9**, 2838–2843.

9 Y. Yin, R. M. Rioux, C. K. Erdonmez, S. Hughes, G. A. Somorjai and A. P. Alivisatos, *Science*, 2004, **304**, 711–714.

10 B. D. Anderson and J. B. Tracy, *Nanoscale*, 2014, DOI: 10.1039/C1034NR02025A.

11 H. J. Fan, U. Gösele and M. Zacharias, *Small*, 2007, **3**, 1660–1671.

12 A. Cabot, R. K. Smith, Y. Yin, H. Zheng, B. M. Reinhard, H. Liu and A. P. Alivisatos, *ACS Nano*, 2008, **2**, 1452–1458.

13 A. Cabot, V. F. Puntes, E. Shevchenko, Y. Yin, L. Balcells, M. A. Marcus, S. M. Hughes and A. P. Alivisatos, *J. Am. Chem. Soc.*, 2007, **129**, 10358–10360.

14 Y. Ma, K. Huo, Q. Wu, Y. Lu, Y. Hu, Z. Hu and Y. Chen, *J. Mater. Chem.*, 2006, **16**, 2834–2838.

15 R. K. Chiang and R. T. Chiang, *Inorg. Chem.*, 2006, **46**, 369–371.

16 G. Xiao, Y. Zeng, Y. Jiang, J. Ning, W. Zheng, B. Liu, X. Chen, G. Zou and B. Zou, *Small*, 2013, **9**, 793–799.

17 A. D. Smigelskas and E. O. Kirkendall, *Trans. Am. Inst. Mining Metallurg. Eng.*, 1947, **171**, 130–142.

18 W. Wang, M. Dahl and Y. Yin, *Chem. Mater.*, 2012, **25**, 1179–1189.

19 H. J. Fan, M. Knez, R. Scholz, K. Nielsch, E. Pippel, D. Hesse, M. Zacharias and U. Gösele, *Nat. Mater.*, 2006, **5**, 627–631.

20 B. Liu and H. C. Zeng, *J. Am. Chem. Soc.*, 2004, **126**, 16744–16746.

21 Y. Yin, C. K. Erdonmez, A. Cabot, S. Hughes and A. P. Alivisatos, *Adv. Funct. Mater.*, 2006, **16**, 1389–1399.

22 S. Kim, Y. Yin, A. P. Alivisatos, G. A. Somorjai and J. T. Yates, *J. Am. Chem. Soc.*, 2007, **129**, 9510–9513.

23 J. Gao, G. Liang, B. Zhang, Y. Kuang, X. Zhang and B. Xu, *J. Am. Chem. Soc.*, 2007, **129**, 1428–1433.

24 E. V. Shevchenko, M. I. Bodnarchuk, M. V. Kovalenko, D. V. Talapin, R. K. Smith, S. Aloni, W. Heiss and A. P. Alivisatos, *Adv. Mater.*, 2008, **20**, 4323–4329.

25 S. H. Choi, H. B. Na, Y. I. Park, K. An, S. G. Kwon, Y. Jang, M. H. Park, J. Moon, J. S. Son, I. C. Song, W. K. Moon and T. Hyeon, *J. Am. Chem. Soc.*, 2008, **130**, 15573–15580.

26 H. Kim, M. Achermann, L. P. Balet, J. A. Hollingsworth and V. I. Klimov, *J. Am. Chem. Soc.*, 2004, **127**, 544–546.

27 X. Wang, X. Kong, Y. Yu and H. Zhang, *J. Phys. Chem. C*, 2007, **111**, 3836–3841.

28 T. Hirakawa and P. V. Kamat, *J. Am. Chem. Soc.*, 2005, **127**, 3928–3934.

29 K. Y. Niu, J. Park, H. M. Zheng and A. P. Aivisatos, *Nano Lett.*, 2013, **13**, 5715–5719.

30 C. M. Wang, A. Genc, H. Cheng, L. Pullan, D. R. Baer and S. M. Bruemmer, *Sci. Rep.*, 2014, **4**, 3683.

31 S. J. Pennycook, *Ultramicroscopy*, 1989, **30**, 58–69.

32 P. D. Nellist and S. J. Pennycook, *Adv. Imaging Electron Phys.*, 2000, **113**, 147–203.

33 J. Zhu, Y. Shen, A. Xie and L. Zhu, *J. Mater. Chem.*, 2009, **19**, 8871–8875.

34 C. H. B. Ng, H. Tan and W. Y. Fan, *Langmuir*, 2006, **22**, 9712–9717.

35 H. Tan, S. Li and W. Y. Fan, *J. Phys. Chem. B*, 2006, **110**, 15812–15816.

36 J. Lian, K. Anggara, M. Lin and Y. Chan, *Small*, 2014, **10**, 667–673.

37 H. G. Liao, K. Niu and H. Zheng, *Chem. Commun.*, 2013, **49**, 11720–11727.

38 A. H. Latham and M. E. Williams, *Langmuir*, 2008, **24**, 14195–14202.

39 W. Feng, L. D. Sun, Y. W. Zhang and C. H. Yan, *Small*, 2009, **5**, 2057–2060.

40 A. A. El Mel, L. Molina-Luna, M. Buffiere, P. Y. Tessier, K. Du, C. H. Choi, H. J. Kleebe, S. Konstantinidis, C. Bittencourt and R. Snyders, *ACS Nano*, 2014, **8**, 1854–1861.

41 Z. Yang, M. Walls, I. Lisiecki and M.-P. Pileni, *Chem. Mater.*, 2013, **25**, 2372–2377.

42 D. B. Mawhinney and J. T. Yates Jr., *Carbon*, 2001, **39**, 1167–1173.

43 W. C. Mallard, R. F. Bass, L. M. Slifkin and A. B. Gardner, *Phys. Rev.*, 1963, **129**, 617–625.

44 J. L. White, R. L. Orr and R. Hultgren, *Acta Metallurg.*, 1957, **5**, 747–760.

45 M. A. Asoro, D. Kovar and P. J. Ferreira, *ACS Nano*, 2013, **7**, 7844–7852.

46 N. Lu, J. Wang, S. Xie, Y. Xia and M. J. Kim, *Chem. Commun.*, 2013, **49**, 11806–11808.

47 G. I. N. Waterhouse, G. A. Bowmaker and J. B. Metson, *Phys. Chem. Chem. Phys.*, 2001, **3**, 3838–3845.

48 B. V. L'Vov, *Thermochim. Acta*, 1999, **333**, 13–19.

49 P. J. Herley and E. G. Prout, *J. Am. Chem. Soc.*, 1960, **82**, 1540–1543.

50 H. J. Bi, W. P. Cai, L. D. Zhang, D. Martin and F. Trager, *Appl. Phys. Lett.*, 2002, **81**, 5222–5224.

51 K. N. Tu and U. Gösele, *Appl. Phys. Lett.*, 2005, **86**, 093111.

52 R. Nakamura, D. Tokozakura, J. G. Lee, H. Mori and H. Nakajima, *Acta Mater.*, 2008, **56**, 5276–5284.

53 W. Wu and M. M. Maye, *Small*, 2014, **10**, 271–276.

54 R. Ji, L. Wang, L. Yu, B. Geng, G. Wang and X. Zhang, *ACS Appl. Mater. Interfaces*, 2013, **5**, 10465–10472.

55 B. Fang, A. Gu, G. Wang, W. Wang, Y. Feng, C. Zhang and X. Zhang, *ACS Appl. Mater. Interfaces*, 2009, **1**, 2829–2834.

56 X. Wang, H. F. Wu, Q. Kuang, R. B. Huang, Z. X. Xie and L. S. Zheng, *Langmuir*, 2010, **26**, 2774–2778.

57 Y. Ida, S. Watase, T. Shinagawa, M. Watanabe, M. Chigane, M. Inaba, A. Tasaka and M. Izaki, *Chem. Mater.*, 2008, **20**, 1254–1256.

58 M. M. Rahman, S. B. Khan, A. Jamal, M. Faisal and A. M. Asiri, *Microchim. Acta*, 2012, **178**, 99–106.